Neutron capture cross sections of the cerium isotopes for *s*- and *p*-process studies

F. Käppeler, K. A. Toukan,* and M. Schumann
Forschungszentrum Karlsruhe, Institut für Kernphysik, Postfach 3640, D-76021 Karlsruhe, Germany

A. Mengoni
Comitato Nazionale per la Ricerca e per lo Sviluppo dell'Energia Nucleare e delle Energie Alternative (ENEA), Settore Fisica Applicata, V. Ercolani 8, I-40138 Bologna, Italy

(Received 10 October 1995)

The neutron capture cross sections of the stable cerium isotopes 136, 138, 140, and 142 have been measured relative to that of gold by means of the activation method. The samples were irradiated in a quasistellar neutron spectrum for $kT=25$ keV using the ^{7}Li$(p,n)^{7}$Be reaction near threshold. Variation of the experimental conditions in different activations and the use of different samples allowed for the reliable determination of corrections and the evaluation of systematic uncertainties. The resulting stellar cross sections can be given with uncertainties between 3% and 7%. The present data for ^{136}Ce and ^{138}Ce are the first experimental information in this mass region of relevance for *p*-process studies to our knowledge, whereas the new ^{142}Ce cross section allowed to resolve a previous discrepancy. The experimental results are complemented by a set of calculated cross sections for all cerium isotopes from ^{132}Ce to ^{142}Ce as well as for ^{141}Pr, ^{142}Pr, and ^{143}Pr. The improved cross sections were used in an updated *s*-process analysis of the Ce-Pr-Nd region that included the small branchings at ^{141}Ce and ^{142}Pr. The consequences of the resulting *s* abundances are discussed with respect to isotopic anomalies in meteoritic neodymium as well as for the *r*- and *p*-process residuals.

PACS number(s): 25.40.Lw, 26.20.+f, 26.30.+k, 27.60.+j

I. INTRODUCTION

The present interest in the (n,γ) cross sections of the cerium isotopes is motivated by two aspects. These cross sections allow to study the influence of the *s*-process branchings at ^{141}Ce and ^{142}Pr, while the complete set of stellar (n,γ) rates for the stable cerium isotopes may be used to test the calculated input data for *p*-process calculations in this mass region. The *s*-process branchings are important for determining the *s* contributions to ^{142}Ce and ^{142}Nd in order to obtain the respective *r*- and *p*-process components.

The *s*-process reaction flow exhibits small branchings at ^{141}Ce and ^{142}Pr. These branchings cause part of the *s*-process reaction flow between ^{140}Ce and ^{146}Nd to bypass ^{142}Nd (see Fig. 1). Since ^{142}Nd is shielded against the *r*-process β decays by ^{142}Ce, it could be considered as an *s*-only isotope, provided that *p*-process contributions are negligible. Then, the branching probabilities follow from the comparison of the empirical product, $\langle\sigma\rangle N_s(^{142}\mathrm{Nd})$ of the stellar neutron capture cross section and the ^{142}Nd abundance with the well established $\langle\sigma\rangle N_s$ systematics in the mass region between the reliable normalization points ^{124}Te and ^{150}Sm [1]. Because the stellar decay rates of ^{141}Ce and ^{142}Pr are almost independent of temperature [2], the branchings at $A=141$, 142 could be analyzed in terms of the *s*-process neutron density.

So far, these branchings have not received much attention because the expected branching factor of about 5% was completely masked by the 9% uncertainty of the ^{142}Nd cross section which propagates directly to the resulting *s* abundance. However, recent *s*-process studies with significantly improved experimental techniques [3,4] have demonstrated that this uncertainty can be reduced to the 1–2 % level, thus allowing sensitive analyses, even for small branchings.

On the other hand, possible *p*-process contributions can no longer be neglected in such refined analyses. Examination of the subsequent mass region between Nd and Sm [5] showed that the present ^{142}Nd cross section would suggest an 8% *p* contribution to this isotope, even without considering the branchings at $A=141/142$. Since the *s* abundance of ^{142}Nd is reduced if these branchings are included, its *p* contribution would increase to more than 10%, thus becoming as significant as the largest *p* abundances between ^{92}Mo and ^{96}Ru. This comparably large *p* abundance appears plausible in view of the fact that ^{142}Nd is the heaviest neutron magic

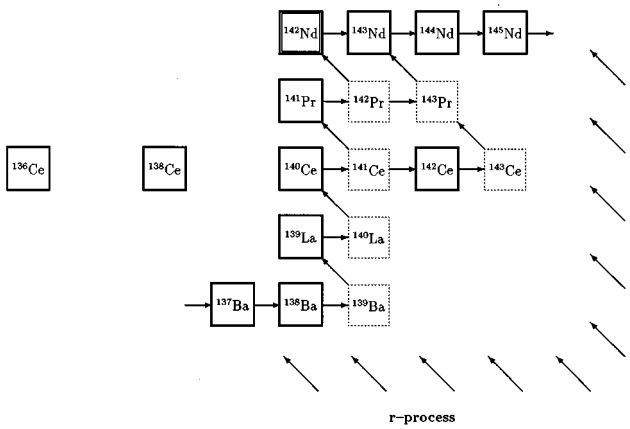

FIG. 1. The *s*-process reaction path in the Ce–Pr–Nd region with the branchings at $A=141/142$.

*On leave from College of Engineering and Technology, The University of Jordan, Amman, Jordan.

nucleus with $N=82$ (as is ^{92}Mo at $N=50$). Therefore, it is favored in a p-process environment where the (γ,n) reaction flow is damped by the higher neutron binding energies. Additionally, ^{142}Nd is further enhanced by the decay of its α-unstable p-process progenitors ^{146}Sm, ^{150}Gd, and ^{156}Dy.

This evidence for a 10% p contribution to ^{142}Nd is also supported by the new generation of p-process studies [6–8]. Such calculations are usually compared to the limited number of p-only isotopes, which are probably not representative of the true abundances near the magic neutron number $N=82$. If a reliable decomposition into its s- and p-process contributions can be achieved by an accurate s-process analysis, ^{142}Nd may provide a further test for the general p-process pattern in this mass region. This is particularly important in view of the many long–lived α emitters of relevance for the interpretation of isotopic anomalies in meteoritic material [9]. Accordingly, the characterization of the s-process flow between cerium and neodymium is a major motivation of the present study.

For a quantitative discussion of the p-process yields, it is important to reduce the uncertainties in these calculations. To a substantial part, these uncertainties originate from the fact that experimental reaction rates are still completely missing in the entire mass region $A>90$. Therefore, the second objective of this study is to establish a complete set of experimental (n,γ) cross sections for the stable cerium isotopes which can be used for testing the systematic trend of the reaction rates in this mass region. These data are expected to provide a sensitive comparison with cross section calculations between ^{132}Ce and ^{142}Ce, in particular with respect to shell effects around magic neutron number $N=82$.

The first part of this paper describes the measurement of the Maxwellian average (n,γ) cross sections of all stable cerium isotopes for a thermal energy of $kT=25$ keV (Secs. II–IV). The measurements are extended in neutron energy and complemented for the unstable isotopes by statistical model calculations. These were based on a new parameter systematics which was evaluated with emphasis on the influence of shell and pairing effects (Sec. V). The resulting improvements for the s-process abundances in the Ce–Pr–Nd branchings are discussed in Sec. VI including the implications for the r- and p-process residuals close to the r-process abundance peak at $A=130$.

II. EXPERIMENTAL TECHNIQUE AND ACTIVATIONS

For the determination of the stellar neutron capture cross sections of ^{136,138,140,142}Ce, samples of natural elemental cerium were irradiated in a quasistellar neutron spectrum. The experimental setup was the same as that described by Beer and Käppeler [10], with the samples directly attached to the respective neutron target. The neutron spectrum is obtained by bombarding 30 μm thick metallic lithium targets of 6 mm diameter with protons of 1912 keV, 31 keV above the reaction threshold. The ^{7}Li$(p,n)^{7}$Be reaction then yields a continuous neutron energy distribution with a high energy cutoff at $E_n=106$ keV. It has been shown that the resulting neutrons are emitted in a forward cone of 120° opening angle. The angle–integrated spectrum peaks at 25 keV and exhibits almost exactly the shape required to determine the proper cross section average $\langle\sigma v\rangle/v_T$ corresponding to the stellar cross section for a thermal energy of $kT=25\pm0.5$ keV [11]. Hence, the reaction rate measured in such a spectrum immediately yields the proper stellar cross section.

The samples consisted of metallic cerium disks 10 mm in diameter and were placed directly on the lithium target. Since cerium is the most reactive of the rare-earth metals and oxidizes readily at room temperature [12], the samples were protected by an argon atmosphere during irradiation. The sample diameter is slightly smaller than the diameter of the neutron cone at the sample position. Consequently, the effective sample thickness was defined by the total mass to ±0.2 %.

The cerium samples were sandwiched between two 0.03 mm thick gold foils of the same diameter. The simultaneous activation of these foils served for normalization to the well known gold cross section which has been determined in an identical neutron spectrum (648 ± 10 mb at $kT=25$ keV [11]). This normalization accounts automatically for the definition of the stellar cross section; to obtain the cross section averaged over the experimental spectrum, the present results have to be multiplied by a factor $\sqrt{\pi}/2$ (for details see Ref.[11]).

The characteristics of all samples used in the six activations are summarized in Table I together with the respective activation schemes. For ^{136}Ce and ^{142}Ce, the activations were carried out by irradiating the samples for ~15 h and subsequently counting the γ-ray lines from the decay of ^{137}Ce and ^{143}Ce ($t_{1/2}=9.0$ h and 33.0 h, respectively). For ^{138}Ce and ^{140}Ce, the irradiations lasted for several days because of the longer-lived product nuclei ^{139}Ce and ^{141}Ce ($t_{1/2}=137.6\,d$ and $32.5\,d$). Nevertheless, the excellent sensitivity of the technique allowed to deduce the cross sections of ^{138}Ce and ^{140}Ce from the shorter irradiations as well. By the variation of the experimental conditions, in particular with respect to sample thickness and irradiation time, the systematic uncertainties of the measurement could be studied experimentally yielding reliable corrections for these parameters.

During all activations the neutron yield was continuously monitored in intervals of 20 s or 1 min for the later correction of the total sample activity, which may originate from time dependencies in the neutron flux. After the irradiations, the induced activities were counted in a low background environment. In the course of activations CE1, CE2, and CE3 these measurements were performed with a 76 cm^3 HPGe detector, but for the last three activations a 175 cm^3 HPGe detector could be used resulting in significantly better counting statistics for the weak lines, in particular for the 447.15 keV line in the decay of ^{137}Ce. The detector efficiencies, ϵ_γ, were calibrated in the energy range $14<E_\gamma<800$ keV with an uncertainty of ±1.5 % using a set of standard sources.

Figure 2 shows the γ-ray spectrum from activation CE6. Due to the extended irradiation and measuring times of 93 h and 24 h, respectively, this example is not optimized for the shorter-lived isotopes. Nevertheless, it exhibits the γ-ray transitions associated with the decay of all cerium isotopes. Neutron capture in the two abundant isotopes ^{140}Ce and ^{142}Ce gives rise to the lines in the spectrum, which are indicated by arrows from above, while the lines related to the rare isotopes ^{136}Ce and ^{138}Ce are marked from below. The

TABLE I. Activation schemes and sample characteristics.

Activations			Samples		
Run	Sample sequence [a]	Irradiation time	Thickness (mm)	Total mass (mg)	Mass density (10^{-4} at/b)
CE1	Au	67.3 h	0.03	41.0±0.1	1.5960
	Ce		0.10	49.1±0.1	^{138}Ce: 0.0067
					^{140}Ce: 2.3773
					^{142}Ce: 0.2976
	Au		0.03	41.6±0.1	1.6194
CE2	Au	118.0 h	0.03	42.3±0.1	1.6466
	Ce		0.10	46.1±0.1	^{138}Ce: 0.0063
					^{140}Ce: 2.2320
					^{142}Ce: 0.2795
	Au		0.03	41.1±0.1	1.5960
CE3	Au	15.25 h	0.03	44.0±0.1	1.7128
	Ce		0.20	95.6±0.14	^{136}Ce: 0.0099
					^{138}Ce: 0.0131
					^{140}Ce: 4.6287
					^{142}Ce: 0.5796
	Au		0.03	46.0±0.1	1.7907
CE4	Au	15.3 h	0.03	42.3±0.1	1.6466
	Ce		0.25	127.2±0.1	^{136}Ce: 0.0132
					^{138}Ce: 0.0174
					^{140}Ce: 6.1586
					^{142}Ce: 0.7712
	Au		0.03	41.2±0.1	1.6038
CE5	Au	18.0 h	0.03	45.7±0.1	1.7790
	Ce		0.25	120.1±0.1	^{136}Ce: 0.0125
					^{138}Ce: 0.0164
					^{140}Ce: 5.8149
					^{142}Ce: 0.7282
	Au		0.03	46.8±0.1	1.8218
CE6	Au	93.0 h	0.03	45.2±0.1	1.7907
	Ce		0.25	125.9±0.1	^{136}Ce: 0.0131
					^{138}Ce: 0.0172
					^{140}Ce: 6.0957
					^{142}Ce: 0.7633
	Au		0.03	46.0±0.1	1.7595

[a]The first listed sample was closest to the neutron target.

respective cross sections were evaluated from the dominant lines for which the transition energies are given explicitly. Only in case of ^{142}Ce, two transitions, the 57.35 keV and the 293.26 keV lines, were used simultaneously as an additional check (see Sec. IV). The gold activity was derived via the well known 411.8 keV transition in ^{198}Hg.

All decay parameters used in the analysis are summarized in Table II [13–17].

III. DATA ANALYSIS

The net counts, C_γ, for each of the peaks in Fig. 2 can be expressed as

$$C_\gamma = A K_\gamma \epsilon_\gamma I_\gamma f_w f_m , \quad (1)$$

where A denotes the total number of activated nuclei at the end of irradiation, K_γ the correction for γ-ray self-

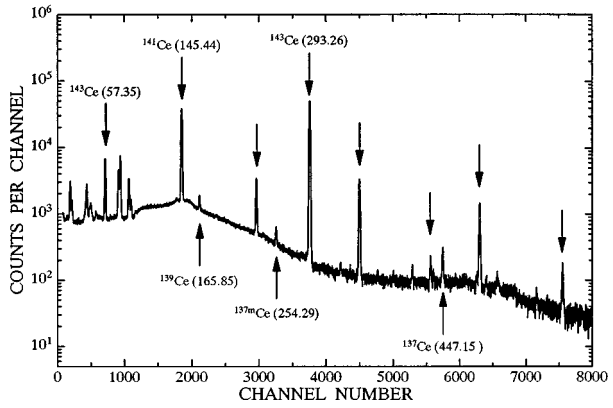

FIG. 2. Gamma-ray spectrum measured after activation CE6. The lines from captures in the abundant and rare isotopes are indicated above and below the spectrum, respectively.

absorption, ϵ_γ the efficiency of the HPGe detector, and I_γ the relative γ-ray intensity per decay. The time factors $f_w = e^{-\lambda t_w}$ and $f_m = (1-e^{-\lambda t_m})$ account for the fraction of nuclei that decay during the waiting time between irradiation and measurement and during the measurement itself and are discussed elsewhere [10]; λ is the decay constant of the respective product nucleus. The corrections for γ-ray self-absorption, K_γ, were calculated with the absorption coefficients of Storm and Israel [18]. The total number of activated nuclei A is given by

$$A = \Phi_{\rm tot} N \sigma f_b , \tag{2}$$

where $\Phi_{\rm tot} = \int \Phi(t) dt$ is the time–integrated neutron flux, N the number of sample atoms per cm^2, and σ the spectrum-averaged neutron capture cross section. The time factor f_b corrects for the decay during activation including the effects due to a time variation of the neutron flux (for a definition see Ref.[10]). Since the neutron flux is determined by the gold foils on both sides of the cerium sample, corrections for target geometry as well as for neutron scattering and self-shielding are accounted for by averaging the induced activities of the two gold foils, which differed by 6 to 7% on average. Hence, the ratio of the activated nuclei in the respective target and reference samples is given to very good accuracy by

$$\frac{A_i}{A_{\rm Au}} = \frac{\sigma_i N_i f_{b,i}}{\sigma_{\rm Au} N_{\rm Au} f_{b,{\rm Au}}} . \tag{3}$$

TABLE II. Decay properties of the product nuclei.

Product nucleus	Half-life	Gamma-ray energy (keV)	Relative intensity per decay (%)
^{137}Ce	9.0±0.3 h	447.15	1.78±0.08 [a]
^{137m}Ce	34.4±0.3 h	254.29	11.0±0.4 [a]
^{139}Ce	137.640±0.023 d	165.85	79.88±0.014 [b]
^{141}Ce	32.501±0.005 d	145.44	48.2±0.3 [c]
^{143}Ce	33.039±0.006 h	293.26	42.8±0.4 [d]
		57.35	11.73±0.36 [d]
^{198}Au	2.696±0.002 d	411.8	95.5±0.1 [e]

[a]Peker [13].
[b]Burrows [14].
[c]Peker [15].
[d]Peker [16].
[e]Auble [17].

In case of the ^{136}Ce cross section, data analysis was complicated by two effects. The decay of the ^{137}Ce ground state is characterized by the 447.15 keV γ-transition (Table II). This line is superimposed by a transition in the decay of ^{143}Ce at $E_\gamma = 447.45$ keV. The corresponding correction of typically 15% of the total peak area was determined by normalizing the ^{143}Ce contribution via the dominant line of this decay at 293.26 keV. Furthermore, the ^{136}Ce cross section is composed of the partial (n,γ) cross sections σ_m to the isomer at 254.29 keV ($t_{1/2} = 34.4$ h) and $\sigma_{\rm gs}$ to the ground state ($t_{1/2} = 9.0$ h). Since the isomer decays predominantly to the ground state, this additional feeding had to be considered in the evaluation of $\sigma_{\rm gs}$ by the following steps:

(i) The correction for the fraction of activated nuclei which decay during the irradiation, f_b, had to be modified by adding the fraction of ^{137m}Ce nuclei that have decayed to the ^{137}Ce ground state during this period t_b. Assuming constant neutron flux during the irradiation, one obtains

$$f_b' = f_b + \frac{\sigma_m}{\sigma_{\rm gs}} \left\{ \frac{(1-e^{-\lambda_2 t_b})}{\lambda_2 t_b} - \frac{(e^{-\lambda_1 t_b} - e^{-\lambda_2 t_b})}{(\lambda_2 - \lambda_1) t_b} \right\}, \tag{4}$$

where λ_1 and λ_2 are the decay constants of ^{137m}Ce and ^{137}Ce, respectively. Since this correction factor was only about 1.8%, the influence of neutron flux variations during t_b was neglected.

(ii) Accordingly, the fraction of ^{137m}Ce that has decayed to the ground state during the waiting time t_w had to be considered as well. This correction

$$f_w' = f_w + \frac{\sigma_m f_{b,m}}{\sigma_{\rm gs} f_{b,{\rm gs}}} \left\{ \frac{e^{-\lambda_1 t_w} - e^{-\lambda_2 t_w}}{(\lambda_2 - \lambda_1)} \right\} \lambda_1 \tag{5}$$

is typically less than 0.4% for the present measurements.

(iii) At last, the number of counts in the 447.15 keV line of the ground state decay had to be corrected for the contribution due to the decay of the isomer during the counting period. This correction was determined via the 254.29 keV transition from the decay of the isomer (Table II) by considering the relative intensities, self–absorption corrections, and detector efficiencies of the 447.15 keV and 254.29 keV lines. The resulting contribution of the isomer decay is then

$$C_\gamma(447) = C_\gamma(254) \frac{\epsilon_\gamma(447) I_\gamma(447) K_\gamma(447)}{\epsilon_\gamma(254) I_\gamma(254) K_\gamma(254)} F(t_m), \tag{6a}$$

where $F(t_m)$ represents the fraction of nuclei in the ground state which originated from the isomer decay and decayed during the counting period,

$$F(t_m) = \left(1 + \frac{\lambda_1 e^{-\lambda_2 t_m}}{\lambda_2 - \lambda_1} - \frac{\lambda_2 e^{-\lambda_1 t_m}}{\lambda_2 - \lambda_1} \right) \Big/ (1 - e^{-\lambda_1 t_m}). \tag{6b}$$

TABLE III. Compilation of uncertainties.

Source of uncertainty	Uncertainty (%)					
	Au	^{137gs}Ce	^{137m}Ce	^{139}Ce	^{141}Ce	^{143}Ce
Gold cross section	1.5	. . .	. . .	. . .	. . .	. . .
Sample thickness	0.2	0.2	0.2	0.2	0.2	0.2
Time factors, f_w, f_m, f_b	<0.4	0.6 – 4.0	<0.5	<0.4	<0.4	<0.5
Counting statistics	<0.4	2.5 – 10	2.5 – 17	0.9 – 5.5	<0.2	<0.3
Self-absorption K_γ	0.03	<0.3	<0.1	<0.6	<0.8	<0.18
Efficiency ratio for Ce and Au γ–ray lines	. . .	1.5	1.5	1.5	1.5	1.5
Gamma-ray intensity per decay I_γ	0.1	4.5	3.6	0.02	0.62	0.93
Difference in neutron flux	. . .	<2.4	<2.4	<2.4	<2.4	<2.4
Spectrum cutoff at 106 keV	. . .	1.0	1.0	1.0	1.5	1.5
Total uncertainty ($kT=25$ keV)						
CE1	. . .	. . .	17.5	4.6	3.6	4.2
CE2	. . .	. . .	. . .	3.4	3.5	3.4
CE3	. . .	13.6	13.3	4.4	3.6	4.0
CE4	. . .	7.4	7.5	6.5	3.4	4.2
CE5	. . .	8.0	7.2	4.2	3.8	3.8
CE6	. . .	8.0	6.0	2.8	3.2	3.2
Extrapolation to $kT=20$ and 30 keV	. . .	0.8	0.8	0.8	1.2	1.2
Extrapolation to $kT=10$ and 50 keV	. . .	3.0	3.0	3.0	4.0	4.0

For a counting time of 28 h, the decay of the isomer requires a 5% correction for the measured intensity of the 447.15 keV line.

IV. RESULTS

The experimental uncertainties are summarized in Table III. The investigated reactions are indicated by the respective product nuclei. For ^{136}Ce the partial cross sections to the isomer and to the ground state in ^{137}Ce are listed separately.

Apart from the gold reference cross section, a first significant uncertainty occurs in the time factor f_b for the partial cross section of ^{136}Ce to the ground state in ^{137}Ce during activation CE6. This activation lasted for 93 h, which is 10 times the half-life of that state; thus, the relatively small uncertainty of the half-life results in the 4% uncertainty in the time factor. In all other activations, this uncertainty was much smaller since the irradiation times were better matched to the respective half-lives.

The largest uncertainties are due to counting statistics from the induced activities of the rare isotopes. In particular, this holds for ^{136}Ce where the relative γ-ray intensities are small. The 10% to 12% uncertainties for the decay of ^{137gs}Ce and ^{137m}Ce refer to activation CE3 and could be reduced to less than 7% in the later activations.

The uncertainty introduced by the relative γ-ray intensities affects again the rare isotopes. With the data given in Table II, any future improvement of these values will allow to improve the respective cross sections accordingly. The effect of the difference in neutron flux between the gold foils and the cerium sample was estimated from the two values measured with the gold foils, 20% of that difference being assumed as the corresponding uncertainty.

Though the experimental spectrum represents a very good approximation of the thermal situation, the cutoff at 106 keV requires a small correction in case that the respective cerium cross sections exhibit a different energy dependence than the gold reference cross section. This problem of the cross section shape with neutron energy affects also the extrapolation of the measured 25 keV cross sections to other thermal energies, in particular to $kT=30$ keV which is commonly used for the comparison of s-process cross sections. Since differential (n,γ) cross sections, $\sigma_{n,\gamma}(E_n)$, are almost completely missing for the cerium isotopes [19], this information has been adopted from the calculated cross sections presented in the following section. The related uncertainties were estimated by comparison with a simple $1/v$ dependence. While this procedure might be adequate for ^{136}Ce and ^{138}Ce, the neutron magic isotope ^{140}Ce and probably also ^{142}Ce are expected to exhibit pronounced structure in their cross sections because of the much lower level densities in the respective compound nuclei. Since this structure is not described by the statistical model calculations, correspondingly larger uncertainties have been adopted in extrapolating the cross sections of these two isotopes. The total uncertainties for the 25 keV cross sections obtained from the six activations have been determined by adding the systematic uncertainties in quadrature.

The resulting cross sections from the various activations are summarized in Table IV. The differences among the data obtained in different activations are well within the estimated uncertainties, thus confirming the procedures applied in data analysis.

The comparison to previous experiments is restricted to ^{140}Ce and ^{142}Ce since the lighter cerium isotopes have been investigated for the first time to our knowledge. Apart from

TABLE IV. Measured stellar (n,γ) cross sections of ^{136}Ce, ^{138}Ce, ^{140}Ce, and ^{142}Ce compared with previous experimental data.

Thermal energy (keV)	$\langle\sigma v\rangle/v_T$ (mb)				
	^{136}Ce$\rightarrow^{137gs}$Ce	^{136}Ce$\rightarrow^{137m}$Ce	^{138}Ce	^{140}Ce	^{142}Ce
	Previous data				
30	100 [a]	...	30 [a]	3±3 [a]	360±60 [a]
	...	...	...	23±4 [b]	55±9 [b]
	...	...	...	7.3±4 [c]	17.3±8 [c]
	...	...	...	7.7±0.9 [d]	...
	...	...	...	10.6±0.5 [e]	18.1±1.1 [e]
	...	...	...	13.6±1.0 [f]	30.8±2.0 [f]
	This work				
25					
CE1	...	27.7±4.9	191±9	12.4±0.5	31.1±1.3
CE2	...	...	215±8	13.0±0.5	31.6±1.1
CE3	330±45	27.1±3.6	192±9	12.4±0.5	31.7±1.3
CE4	326±24	33.4±2.5	170±11	11.1±0.4	29.1±1.2
CE5	326±26	30.7±2.2	202±9	11.8±0.5	30.8±1.2
CE6	312±25	33.6±2.0	185±5	11.1±0.4	30.4±1.0
Mean value	322±21	32.6±1.7	193±5	12.0±0.4	30.8±1.0
30	300±21	28.2±1.6	179±5	11.0±0.4	28.3±1.0

[a]Allen *et al.* [22].
[b]Siddappa *et al.* [23] after renormalization [24].
[c]Anand *et al.* [25].
[d]Musgrove *et al.* [21].
[e]Beer and Käppeler [10].
[f]Xia *et al.* [20], normalized to ^{197}Au cross section used in this work.

the values reported by Xia *et al.* [20], none of the other data are in satisfactory agreement with the present results, neither the differential measurement of Musgrove *et al.* [21] nor the similar activation of Beer and Käppeler [10]. Among the older data, the values quoted in Ref. [22] can be ruled out. The fact that the results of Siddappa *et al.* [23,24] and Anand *et al.* [25] exhibit at least the proper ratio $\sigma(142)/\sigma(140) \approx 2.5$ indicates problems with the characterization of the samples in these experiments, which might be responsible for the observed discrepancies in the absolute cross sections.

The present results for ^{140}Ce and ^{142}Ce are compared in Figs. 3 and 4 to previous experiments (squares) and calculations (circles). These plots illustrate the large uncertainties in the older data as well as the systematic differences in the theoretical results. The two measurements that claimed comparable accuracy for both cross sections [10,20] agree for ^{140}Ce within uncertainties, but the ^{142}Ce cross section of Ref. [10] exhibits a severe discrepancy, which is particularly irritating in view of the perfect agreement obtained for the simultaneously determined ^{140}Ce cross section. A minor part of the discrepancy can be removed by adopting the present γ-ray intensity, $I_\gamma = 42.8\,\%$ for the 293.26 keV line, instead of the 51.37% used in the older measurement. Nevertheless, the revised cross section of 21.7 ± 1.3 mb is still incompatible with the 28.3 ± 1.0 mb obtained in this work.

Therefore, this point has been examined by two additional tests. The ^{142}Ce cross section was also evaluated via the 57.35 keV line, which implied not only a different relative intensity per decay (Table II), but also very different detector efficiencies and self-absorption corrections. Because of the lower γ-ray energy, this analysis was carried out for activations CE1 and CE2 only, where the thinnest cerium samples were used. The result obtained via the 293.26 keV line was

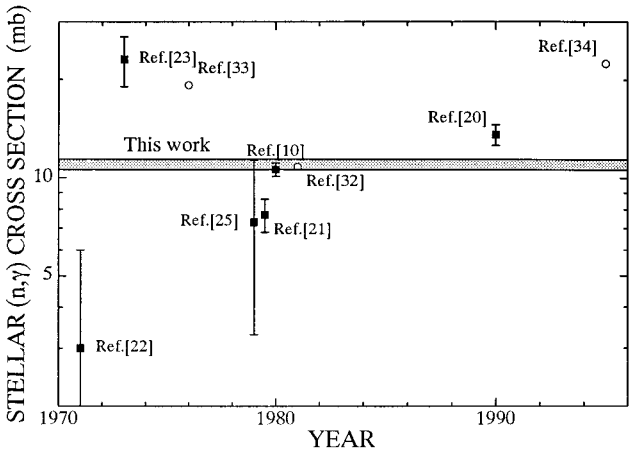

FIG. 3. The new stellar cross section of ^{140}Ce for $kT = 25$ keV compared to previous results.

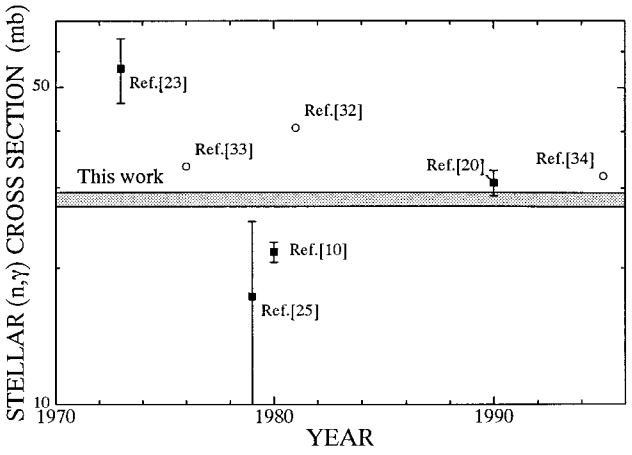

FIG. 4. The new stellar cross section of ^{142}Ce for $kT=25$ keV compared to previous results.

confirmed within the estimated 5% uncertainty of the self-absorption correction. Furthermore, the decay of ^{143}Ce was checked by monitoring the 293.26 keV line during the analysis of activation CE5. Following the decay over 115 h, the half-life was reproduced with an accuracy of ± 0.2 % which corresponds to the counting statistics. Therefore, any interfering background component could be excluded for this γ-ray line.

The (n,γ) cross section of ^{142}Ce could be deduced from all six activations which were carried out under widely different conditions concerning the irradiations (duration and neutron flux) as well as the activity counting (sample thickness, detector efficiency, γ-ray line, waiting and measurement times). Since all these results are consistent within the respective uncertainties, and in view of the agreement with the result of Xia *et al.* [20], there is good reason to adopt the present ^{142}Ce cross section in further *s*-process studies.

V. CALCULATIONS

The experimental data for the stable cerium isotopes have been complemented by model calculations in order to obtain the cross sections for the unstable branch point nuclei ^{141}Ce and ^{142}Pr, which are required for describing the reaction flow in the *s* process. In addition, the complete isotope sequence from ^{132}Ce to ^{142}Ce was investigated for providing an improved data set for *p*-process studies. The calculations were carried out by means of the statistical model based on the Hauser-Feshbach theory. Neutron and γ-ray transmission coefficients were determined using the latest version of the CASTHY code [26] with the following input data.

The optical model potential for the neutron channel as well as the correction for level-width fluctuations were based on the work of Moldauer [27,28].

The γ-ray transmission coefficients were obtained via the giant dipole resonance (GDR) model using $E_R=15.05$ MeV, $\Gamma_R=4$ MeV, and $\sigma_R=320$ mb for the position, width, and peak cross section of the GDR. These parameters were derived from the compilation of Dietrich and Berman [30]. The energy of the GDR has been fixed for mass number $A=140$, and was scaled with a $A^{-1/3}$– dependence for the other isotopes. The width, Γ_R, as well as the peak cross section, σ_R, have been kept constant in all cases except for the target nucleus ^{140}Ce where the cross section had to be reduced to 120 mb in order to reproduce the experimental radiative width $\Gamma_\gamma = 35\pm 9$ meV [29]. The corresponding values for the two praseodymium isotopes were $E_R=15.19$ MeV, $\Gamma_R=5.0$ MeV, and $\sigma_R=338$ mb [30].

The level density calculations were carried out according to the Gilbert-Cameron prescription which implies a Fermi-gas model at high excitation starting around the neutron binding energy and a constant temperature approach for the low energy part. Particular care was devoted to the evaluation of the level density parameters a. This was important because experimental information on the level spacing of neutron resonances existed only for the neutron reactions on ^{140}Ce and ^{141}Pr [29]. Hence, the cross section calculations for all other isotopes had to rely on the parameter systematics for a. This systematics was adopted from the recent work by Mengoni and Nakajima [31] where the essential parameter for the Fermi-gas model, a^*, has been shown to vary smoothly with mass number according to

$$a^* = \alpha A(1-\beta A^{-1/3}). \tag{7}$$

This parameter is related to the average spacing of the single-particle states around the Fermi energy g_F by

$$a = a^*\left(1+\frac{E_{\rm sh}}{U}(1-e^{-\gamma U})\right), \quad a=\frac{\pi^2}{6}g_F, \tag{8}$$

where U denotes the excitation energy and $E_{\rm sh}$ the shell correction energy. The systematic behavior of a^* has been established by due consideration of pairing and shell effects, thus determining the numerical constants α, β, and γ. The relevant parameters obtained with this technique are listed in Table V with the definitions given in Ref. [31].

The present results are listed in Tables VI and VII as Maxwellian averaged cross sections for an extended range of thermal energies between $kT=10$ and 100 keV, which covers the temperature regimes of the *s* and of the *p* process.

The uncertainties of the calculated (n,γ) cross sections are mainly determined by three contributions.

(i) *Optical Model Parameters (OMP):* The reliability of the OMP has been tested with respect to existing total and elastic cross section data. Though a detailed comparison remains unsatisfactory, since these cross sections are strongly fluctuating in the keV region, one finds that the experimental results are reasonably reproduced on average. This suggests a 10% contribution to the overall uncertainty due the OMP's.

(ii) *The Giant Dipole Resonance:* The GDR parameters are expected to vary smoothly for the isotopes under investigation, which are essentially all spherical. Their contributions to the uncertainties are estimated to range between 10 and 20%.

(iii) *Level density:* The capture cross sections are approximately proportional to the inverse of the average level spacing $\langle D\rangle$. From the Fermi–gas model follows

TABLE V. Statistical model parameters.

Compound nucleus	a^* (MeV^{-1})	a (MeV^{-1})	E_{sh} (MeV)	σ^2	T (MeV)	$\langle D\rangle_{l=0}$ (keV)	Γ_γ [a] (eV)
^{132}Ce	16.2	18.2	2.05	36.3	0.77	0.0088	
^{133}Ce	17.0	19.1	2.04	33.1	0.69	0.0112	0.032
^{134}Ce	16.5	17.9	1.50	37.0	0.76	0.0008	0.039
^{135}Ce	17.2	18.6	1.33	33.6	0.68	0.0251	0.034
^{136}Ce	16.7	19.1	2.34	32.8	0.70	0.0076	0.079
^{137}Ce	17.4	17.9	0.47	34.3	0.68	0.0666	0.042
^{138}Ce	16.9	16.5	−0.42	39.4	0.77	0.0096	0.143
^{139}Ce	17.6	16.4	−1.15	37.0	0.71	0.187	0.059
^{140}Ce	17.1	15.1	−1.95	41.0	0.78	0.0505	0.353
^{141}Ce	17.8	16.6	−1.08	32.1	0.60	2.99	
	17.7	16.4				3.2 ± 0.2 [b]	0.039
^{142}Ce	17.3	16.4	−0.32	34.2	0.64	0.130	0.063
^{143}Ce	18.0	18.5	0.41	30.0	0.55	1.72	0.051

[a]Since Γ_γ is a compound-nucleus quantity it is given only for the cases considered in the (n,γ) calculations.
[b]The only experimental $\langle D\rangle_{l=0}$ value [29].

TABLE VI. Calculated stellar (n,γ) cross sections of the cerium isotopes.

Thermal energy	$\langle\sigma v\rangle/v_T$ (mb)										
(keV)	^{132}Ce	^{133}Ce	^{134}Ce	^{135}Ce	^{136}Ce	^{137}C e	^{138}Ce	^{139}Ce	^{140}Ce	^{141}Ce	^{142}Ce
Previous calculations											
30	...	...	...	...	629 [a]	1900 [a]	137 [a]	514 [a]	19.2 [a]	167 [a]	33.4 [a]
	...	...	...	...	398 [b]	...	256 [b]	...	10.8 [b]	...	40.6 [b]
	1632 [c]	3617 [c]	976 [c]	2749 [c]	528 [c]	1170 [c]	243 [c]	281 [c]	22.4 [c]	162 [c]	31.9 [c]
This work											
10	1095	2996	720	1664	441	1943	281	1277	26.8	186	52.9
20	796	2106	516	1151	314	1304	199	842	18.5	118	37.1
25	725	1902	467	1026	283	1155	179	742	16.5	102	33.4
30	674	1759	433	938	262	1051	166	672	15.1	91.0	30.7
40	609	1568	390	816	235	914	149	580	13.1	76.3	27.1
50	567	1440	362	733	218	825	138	521	12.0	66.9	24.8
60	537	1344	343	672	207	761	131	479	11.1	60.2	23.0
70	513	1268	329	623	198	711	125	447	10.4	55.2	21.7
80	493	1203	317	682	191	670	120	420	9.9	51.1	20.6
90	475	1147	307	547	185	636	116	398	9.4	47.8	19.7
100	459	1098	297	517	180	606	113	379	9.1	45.0	18.9
150	402	925	264	414	162	500	101	314	8.1	36.3	16.2
200	369	821	242	355	151	436	94.5	277	7.8	32.1	14.7
250	349	752	227	320	144	392	90.9	254	7.8	29.6	13.6
300	338	700	215	298	139	360	88.7	237	8.0	28.1	12.7
350	333	660	206	283	135	335	87.5	225	8.2	27.0	12.0
400	332	627	198	272	132	314	86.7	214	8.4	26.1	11.4
450	335	599	191	265	129	297	86.2	205	8.5	25.4	10.9
500	339	574	184	258	127	283	85.8	198	8.6	24.6	10.5

[a]Holmes *et al.* [33].
[b]Harris [32].
[c]Rayet [34].

TABLE VII. Calculated stellar (n,γ) cross sections of ^{141}Pr, ^{142}Pr, and ^{143}Pr.

	$\langle\sigma v\rangle/v_T$ (mb)		
Thermal energy (keV)	^{141}Pr	^{142}Pr	^{143}Pr
	Previous data		
30	119±15 [a]	...	...
	162 [b]	932 [b]	645 [b]
	73.8 [c]	...	...
	148 [d]	428 [d]	259 [d]
	This work		
10	196	684	410
20	126	409	264
25	109	343	230
30	97	297	205
40	82	236	172
50	71	197	151
60	63	169	136
70	57	148	124
80	53	131	115
90	49	118	107
100	45	107	101
150	34	74	80
200	29	56	69
250	26	46	61
300	24	40	55
350	23	35	51
400	22	32	48
450	21	30	45
500	20	28	42

[a]Taylor *et al.* [35].
[b]Holmes *et al.* [33].
[c]Harris [32].
[d]Rayet [34].

$$\frac{\delta\langle D\rangle}{\langle D\rangle}=\frac{1-4\sqrt{aU}}{4}\,\frac{\delta a}{a}\approx\sqrt{aU}\frac{\delta a}{a}. \tag{9}$$

The uncertainty of the adopted level spacing can only be estimated for ^{141}Ce where experimental data are available. According to Table V, this comparison yields an uncertainty $\Delta a=0.2\ \mathrm{MeV}^{-1}$ which suggests a 10% uncertainty for $\langle D\rangle$. However, uncertainties around $\Delta a=0.4\ \mathrm{MeV}^{-1}$ might be more realistic as one moves along the isotope chain to ^{132}Ce resulting in uncertainties of 20 to 25 % for the level spacings.

In total, these contributions add to overall cross section uncertainties between 25% near the line of stability and 40% for the most neutron deficient isotopes.

The values from previous calculations are included in Tables VI and VII for $kT=30$ keV showing discrepancies by factors 2–3. For the even-even cerium isotopes, the general trend of the various cross section calculations with mass number is compared in Fig. 5. The present values (thick solid line) are in fairly good agreement with the experimental results, except for ^{140}Ce. However, a 30% discrepancy is not unexpected for this neutron magic nucleus since the basic assumptions for the statistical model are certainly weakened by nuclear structure effects.

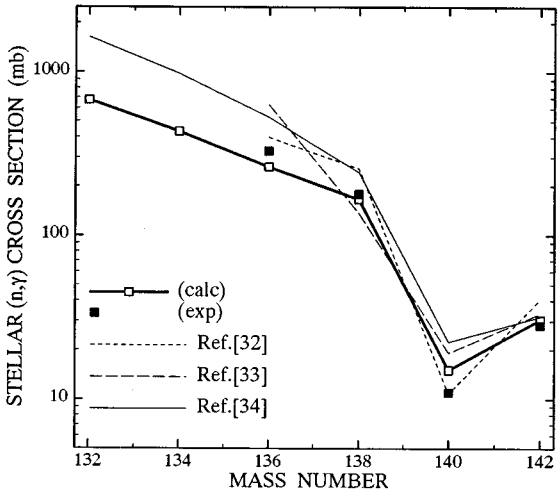

FIG. 5. Calculated Maxwellian averaged capture cross sections of the even cerium isotopes for a thermal energy $kT=30$ keV (solid line) compared to previous calculations (broken lines) and to the present experimental values.

The calculated values of Harris [32] also show good agreement with the experimental data, all cross sections being reproduced within ±30%. This implies that the trend with mass number is properly described, in contrast to the calculations of Holmes *et al.* [33]. In these data, the ^{136}Ce and ^{137}Ce cross sections seem to be systematically overestimated (see also Table VI) which would result in an order of magnitude effect if this trend would be used for extrapolation to the actual p-process region.

Also the more recent calculations of Rayet [34] exhibit a steeper trend with mass number leading to (n,γ) cross sections in the p-process region which are two times larger than the present results (Fig. 5). For the odd cerium isotopes there is a more irregular behavior. In general, the data of Rayet [34] are again about two times larger, but his ^{139}Ce cross section is two times smaller than the present value, while the ^{137}Ce cross sections are almost equal. Since these irregularities correlate with with the level density parameter a, they may originate from difficulties in the global parametrization of shell effects at magic neutron number $N=82$ [34].

The praseodymium cross sections are listed in Table VII. Obviously, the new result for ^{141}Pr compares significantly better to the only experimental value [35] than the two previous calculations [32,33]. Again, the cross sections of Rayet [34] are systematically larger than the present results, but in this case the differences of about 50% are compatible with the respective uncertainties.

In view of the carefully evaluated parameter systematics and the good agreement with the experimental data, the calculated cross sections of this work are recommended to replace the older calculations [24]. They also indicate problems in the global parametrization of recent, comprehensive cross section calculations [34] for updated p-process studies.

TABLE VIII. Abundance contributions of the s, r, and p processes to the mass region between ^{140}Ce and ^{146}Nd.

Isotope	Solar abundance [a] $N_\odot\times10^2$	Classical approach [b] $\langle\sigma\rangle N_s$	$N_s\times10^2$	$N_r\times10^2$	$N_p\times10^2$	Stellar model [b] $N_s\times10^2$
^{140}Ce	100.5±1.7	9.905	88.44±3.45	12.1±3.8	...	92.6
^{141}Pr	16.7±0.40	9.276	(8.17±1.0) [c]	8.53±1.03	...	7.76 [c]
^{142}Ce	12.6±0.21	0.315	1.09±0.04	11.5±0.2	...	1.05
^{142}Nd	22.5±0.29	8.608	(18.43±1.6) [c]	...	4.1±1.6	19.3 [c]
^{143}Nd	10.0±0.13	8.892	(3.62±0.16) [c]	6.50±0.24	...	3.80 [c]
^{144}Nd	19.7±0.26	8.649	7.73±0.44	12.0±0.5	...	8.28
^{145}Nd	6.87±0.09	8.590	1.74±0.36	5.13±0.37	...	1.83
^{146}Nd	14.2±0.18	8.273	9.34±0.46	4.86±0.49	...	8.67

[a]From Ref. [58].
[b]Normalized at ^{150}Sm.
[c]Including the decay of isobars.

Therefore, similar studies in different mass regions are definitely required for a systematic improvement of the cross sections on the proton rich side of the stability valley.

VI. ASTROPHYSICAL IMPLICATIONS

A. The s-process branchings at $A=141, 142$

The neutron capture flow through the s-process branchings at $A=141, 142$ has been analyzed with the new set of Maxwellian averaged cross sections listed in Tables IV, VI, and VII as well as with the neodymium cross sections from the compilation of Bao and Käppeler [24]. Two models were employed in this analysis, the classical approach representing a purely empirical treatment of the s-process [36], and a stellar model associated with helium shell burning in low mass stars [37–39].

The classical steady s-process model [40–42] with the extension for the treatment of branchings in the reaction path [43] represents a useful tool for characterizing the s-process abundances, but also the physical conditions during the s process. A detailed description of the basic features and of the formalism may be found in Refs. [1,36]. The s-process reaction flow was followed as indicated by the solid lines in Fig. 1. The parameters describing the stellar conditions are an exponential distribution of neutron exposures, $\rho(\tau)\sim\exp(-\tau/\tau_0)$, with a mean exposure $\tau_0=0.295\ \mathrm{mb}^{-1}$ at an effective thermal energy of $kT=29$ keV [44], and a mean neutron density of $n_n=(4.1\pm0.6)\times10^8\ \mathrm{cm}^{-3}$ [5].

The s abundances obtained from the classical approach are listed in Table VIII. Compared to estimates based on the older cross sections, the branchings of Fig. 1 are considerably weaker because of the smaller (n,γ) cross sections calculated in this work. The neutron capture probabilities of the branch point isotopes ^{141}Ce, ^{142}Pr, and ^{143}Pr are 4%, 1%, and 4%, respectively. In terms of the reaction flow, however, the branching at ^{143}Pr is completely negligible since it follows the one at ^{142}Pr. Nevertheless, the consequences of the above branchings are significant. They give rise to an s-process contribution of 9±3 % to the observed ^{142}Ce abundance, and they reduce the s abundance of ^{142}Nd by 4% compared to the unbranched situation. The reduction of the s contribution to ^{142}Nd implies a 30% increase of the p-process component for this isotope, which amounts to 18 ±7 %.

This large p component of ^{142}Nd still exhibits a relatively large uncertainty due to the poorly defined s contribution. But with the improved experimental determination of the stellar ^{142}Nd cross section presently under way [45], it will be possible to discuss the resulting consequences in more detail.

B. Isotopic anomalies

The branchings at ^{141}Ce and ^{142}Pr affect also the interpretation of isotopic anomalies that have been discovered in meteoritic neodymium. Such anomalies were first reported by Lugmair *et al.* [46] and interpreted as being due to s-process neodymium by Clayton [47]. While these studies of an acid resistant residue of the Allende meteorite deal with anomalies of a few parts in 1000, much larger effects were found by Zinner *et al.* [48] as well as by Richter *et al.* [49,50] in silicon carbide grains from the Murchison meteorite. The anomalous isotopic pattern of Ref. [49],

$$^{142}\mathrm{Nd}/^{143}\mathrm{Nd}/^{144}\mathrm{Nd}/^{145}\mathrm{Nd}/^{146}\mathrm{Nd}/^{148}\mathrm{Nd}/^{150}\mathrm{Nd}$$
$$=2.13\pm0.08/0.293\pm0.006/$$
$$\equiv1.0/0.161\pm0.005/0.775\pm0.009/0.0281$$
$$\pm0.0058/\equiv0$$

is plotted in Fig. 6 with the s abundances obtained in this work,

$$2.38\pm0.25/0.47\pm0.03/\equiv1.0/0.23\pm0.05/1.21$$
$$\pm0.09/0.046\pm0.009/\equiv0.$$

Compared to the unbranched s-process solution given in Ref. [5] there is now better agreement for the ^{142}Nd/^{144}Nd ratio (Fig. 6), but the discrepancy for the ^{146}Nd/^{144}Nd ratio did not change. It is difficult to comment on this situation as long as the s-process analysis is performed with the rather uncertain cross sections of ^{142}Nd, ^{143}Nd, ^{145}Nd, and ^{144}Nd. For example, a smaller ^{144}Nd cross section would increase the s

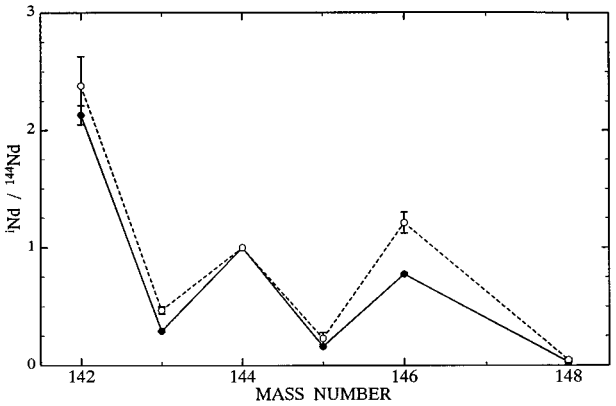

FIG. 6. Comparison of *s*-process neodymium (open circles, this work) with the anomalous abundance pattern reported for SiC inclusions in the Murchison meteorite (filled circles) [49].

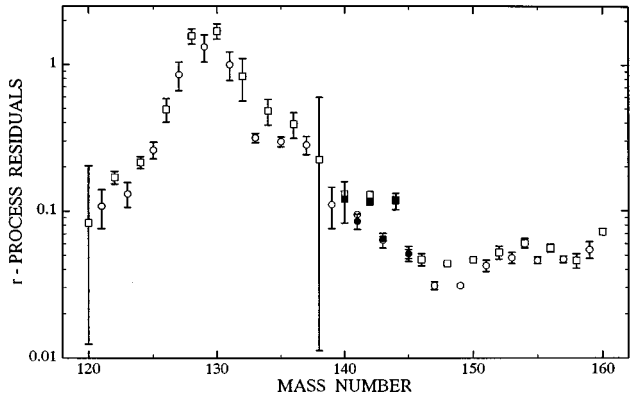

FIG. 7. The *r*-process abundance peak at mass number $A=130$. Values from the present analysis are indicated by black symbols, open symbols refer to the updated results of Ref.[36] (see text).

abundance of this normalization point, which may possibly solve the problem provided that the other Nd cross sections are corrected by corresponding fractions. Therefore, the presently attempted improvement of these data [45] has to be awaited for a final discussion.

The branchings at ^{141}Ce and ^{142}Pr were also studied by means of a stellar *s*-process model. The helium shell burning episodes in thermally pulsing AGB (asymptotic giant branch) stars in the mass range $1<M/M_{\odot}<3$ have been shown to provide the exponential distribution of neutron exposures characteristic of the *main s*-process component [37,38]. It has been shown that the overall *s*-process abundance pattern between Zr and Bi could be reproduced with this model to better than 10% [39,44,51]. This scenario is characterized by two neutron sources. Most of the neutron exposure is provided by the ^{13}C$(\alpha,n)^{16}$O reaction at comparably low neutron densities and temperatures. At the end of the helium burning episode a second neutron source, the ^{22}Ne $(\alpha,n)^{25}$Mg reaction, is activated which leads to a significant modification of the previously produced abundances. In view of the complex time dependence of neutron density and temperature, the *s*-process branchings provide particularly sensitive tests for this model.

The calculations were carried out with the new set of Ce and Pr cross sections using the latest version of the network code NETZ [52] and the neutron density and temperature profiles of the stellar model [53]. The resulting *s*-process abundances are listed in the last column of Table VIII. Compared to the *s* abundances obtained with the classical approach there are no significant differences for the isotopes ^{140}Ce and ^{142}Nd which are characterizing the branchings at $A=141/142$.

If the revised LMS (low mass star) model of Straniero *et al.* [54] is considered, these branchings are much less pronounced. Since the ^{13}C$(\alpha,n)^{16}$O reaction burns already at lower temperatures, the neutron density is reduced by roughly a factor of 10. Accordingly, the ^{142}Ce production is significantly reduced and cannot be compensated during the subsequent neutron exposure from the ^{22}Ne$(\alpha,n)^{25}$Mg reaction because of the relatively small cross sections involved.

C. *r*- and *p*-process abundances

The cross sections determined in this work were used to derive the *r*-process residuals ($N_r=N_{\odot}-N_s$) in the mass range $140<A<146$ (Table VIII). These data contribute to a better characterization of the *r*-process abundance peak at $A=130$ as shown in Fig. 7. Open symbols denote the *r*-process yields of Käppeler *et al.* [36] updated by the recent studies in Refs. [4,5,55]. At A=142 the revised *r* abundance is 9% lower as a result of the now included *s*-process branching at ^{141}Ce, which adds a corresponding *s* component to ^{142}Ce.

Obviously, ^{144}Nd shows a significant deviation from a smooth *r*-process pattern. It is interesting to note that a 40% smaller (n,γ) cross section for ^{144}Nd would remove this discrepancy as well as that in the ^{146}Nd/^{144}Nd ratio of Fig. 6.

For ^{142}Nd, the difference $N_{\odot}-N_s=0.041\pm0.016$ (Table VIII) represents the *p*-process abundance since the *r*-process yield at $A=142$ is accumulated by the stable isobar ^{142}Ce. This corresponds to a *p* contribution of 18 ± 7 %, while recent *p*-process calculations report values between 4% [56,57] and 10% [8]. The stellar *s* process (column 7 of Table VIII) predicts a similar *p*-process yield of 14%, whereas the revised *s*-process model of Straniero *et al.* [54] yields a much smaller *p* contribution in better agreement with the *p*-process models. However, the quantitative discussion of a possible *p*-process peak around $A=142$ must await the improvement of the cross section of ^{142}Nd [45] for a better definition of its *s* abundance.

The consequences of the present (n,γ) cross sections for the abundances of the *p*-only nuclei ^{136}Ce and ^{138}Ce can be estimated in a qualitative way from the work of Rayet *et al.* [6] who investigated the influence of (n,γ) rates on the *p*-process yields by repeating their network calculations with all (n,γ) rates set equal to zero. In this way, the production of ^{136}Ce was found to be strongly reduced while that of ^{138}Ce was increased by a factor of 2, at least in a certain temperature interval. This exercise indicates that the (n,γ) rates are, indeed, important for the final *p*-process yields. Whether the present data would result in an improved isotope pattern in the more realistic model calculations of Prantzos *et al.* [7] still remains to be answered. If possible, an updated calculation should include some experimental information on (p,γ) rates as well.

ACKNOWLEDGMENTS

We thank A. Ernst, E.P. Knaetsch, D. Roller, and W. Seith for their help and support during the neutron irradiations at the Van de Graaff accelerator as well as G. Rupp for his excellent technical assistance throughout the entire experiment. We are also indebted to M. Rayet for providing us with the numerical values of the (n,γ) cross sections used in his *p*-process network. The hospitality of Forschungszentrum Karlsruhe is gratefully acknowledged by K.A.T.

[1] K. Wisshak, F. Voss, F. Käppeler, and G. Reffo, Phys. Rev. C **45**, 2470 (1992).
[2] K. Takahashi and K. Yokoi, Atomic Data Nucl. Data Tables **36**, 375 (1987).
[3] K. Wisshak *et al.*, Phys. Rev. C **48**, 1401 (1993).
[4] F. Käppeler, W. Schanz, K. Wisshak, and G. Reffo, Astrophys. J. **410**, 370 (1993).
[5] K. Toukan, K. Debus, F. Käppeler, and G. Reffo, Phys. Rev. C **51**, 1540 (1995).
[6] M. Rayet, N. Prantzos, and M. Arnould, Astron. Astrophys. **227**, 271 (1990).
[7] N. Prantzos, M. Hashimoto, M. Rayet, and M. Arnould, Astron. Astrophys. **238**, 455 (1990).
[8] W. Howard, B. Meyer, and S. Woosley, Astrophys. J. **373**, L5 (1991).
[9] G. Lugmair and S. Galer, Geochim. Cosmochim. Acta **56**, 1673 (1992).
[10] H. Beer and F. Käppeler, Phys. Rev. C **21**, 534 (1980).
[11] W. Ratynski and F. Käppeler, Phys. Rev. C **37**, 595 (1988).
[12] *Handbook of Chemistry and Physics*, 53rd ed., edited by R. Weast (CRC Press, Cleveland, 1972).
[13] L. Peker, Nucl. Data Sheets **59**, 767 (1990).
[14] T. Burrows, Nucl. Data Sheets **57**, 337 (1989).
[15] L. Peker, Nucl. Data Sheets **45**, 1 (1985).
[16] L. Peker, Nucl. Data Sheets **64**, 429 (1991).
[17] R. Auble, Nucl. Data Sheets **40**, 301 (1983).
[18] E. Storm and H. Israel, Nucl. Data Tables **36**, 375 (1970).
[19] V. McLane, C. Dunford, and P. Rose, in *Neutron Cross Sections* (Academic Press, New York, 1988) Vol. 2.
[20] Y. Xia *et al.*, Chin. J. Nucl. Phys. **12**, 261 (1990).
[21] A. de L. Musgrove, B. Allen, and R. Macklin, Aust. J. Phys. **32**, 213 (1979).
[22] B. Allen, J. Gibbons, and R. Macklin, Adv. Nucl. Phys. **4**, 205 (1971).
[23] K. Siddappa, M. Sriramachandra Murty, and J. Rama Rao, Nuovo Cimento **18A**, 48 (1973).
[24] Z.Y. Bao and F. Käppeler, Atomic Data Nucl. Data Tables **36**, 411 (1987).
[25] R. Anand, M. Jhingan, D. Bhattacharya, and E. Kondaiah, Nuovo Cimento **50A**, 247 (1979).
[26] T. Fukahori and S. Igarasi, Japan Atomic Energy Research Institute Technical report (unpublished).
[27] P. Moldauer, Nucl. Phys. **47**, 65 (1963).
[28] P. Moldauer, Rev. Mod. Phys. **36**, 1079 (1964).
[29] J. Mughabghab, M. Divadeenam, and N. Holden, in *Neutron Cross Sections* (Academic Press, New York, 1981), Vol. 1, Part A.
[30] S. Dietrich and B. Berman, Nucl. Data Atomic Data Tables **38**, 199 (1988).
[31] A. Mengoni and Y. Nakajima, J. Nucl. Sci. Technol. **31**, 151 (1994).
[32] M. Harris, Ap. Space Sci. **77**, 357 (1981).
[33] J. Holmes, S. Woosley, W. Fowler, and B. Zimmerman, Atomic Data Nucl. Data Tables **18**, 305 (1976).
[34] M. Rayet (private communication).
[35] R. Taylor, B. Allen, A. de L. Musgrove, and R. Macklin, Aust. J. Phys. **32**, 551 (1979).
[36] F. Käppeler, H. Beer, and K. Wisshak, Rep. Prog. Phys. **52**, 945 (1989).
[37] I. Iben, Jr. and A. Renzini, Ann. Rev. Astron. Astrophys. **20**, 271 (1983).
[38] D. Hollowell and I. Iben Jr., Astrophys. J. **340**, 966 (1989).
[39] R. Gallino *et al.*, Astrophys. J. **334**, L45 (1988).
[40] E. Burbidge, G. Burbidge, W. Fowler, and F. Hoyle, Rev. Mod. Phys. **29**, 547 (1957).
[41] P. Seeger, W. Fowler, and D. Clayton, Astrophys. J. Suppl. **97**, 121 (1965).
[42] D. Clayton, W. Fowler, T. Hull, and B. Zimmerman, Ann. Phys. **12**, 331 (1961).
[43] R. Ward, M. Newman, and D. Clayton, Astrophys. J. Suppl. **31**, 33 (1976).
[44] F. Käppeler *et al.*, Astrophys. J. **354**, 630 (1990).
[45] K. Wisshak *et al.*, in progress.
[46] G. Lugmair, T. Shimamura, R. Lewis, and E. Anders, Lunar Planet. Sci. **14**, 448 (1983).
[47] D. Clayton, Astrophys. J. **271**, L107 (1983).
[48] E. Zinner, S. Amari, and R. Lewis, Astrophys. J. **382**, L47 (1991).
[49] S. Richter, U. Ott, and F. Begemann, Lunar Planet. Sci. **23**, 1147 (1992).
[50] S. Richter, U. Ott, and F. Begemann, in *Nuclei in the Cosmos '92*, edited by F. Käppeler and K. Wisshak (Institute of Physics, Bristol, 1993), p. 127.
[51] R. Gallino, M. Busso, and C. Raiteri, in *Nuclei in the Cosmos '92*, Ref. [50].
[52] S. Jaag, Diplom thesis, University of Karlsruhe, 1990.
[53] R. Gallino (private communication).
[54] O. Straniero *et al.*, Astrophys. J. **440**, L85 (1995).
[55] F. Voss *et al.*, Forschungszentrum Karlsruhe Technical report (unpublished).
[56] M. Rayet (private communication).
[57] M. Rayet *et al.*, Astron. Astrophys. **298**, 517 (1995).
[58] E. Anders and N. Grevesse, Geochim. Cosmochim. Acta **53**, 197 (1989).